PCCP

ROYAL SOCIETY OF CHEMISTRY

PAPER

Cite this: *Phys. Chem. Chem. Phys.*, 2024, **26**, 21697

Dynamics and thermochemistry of the negatively charged clusters in a 2-hydroxyethylhydrazinium nitrate ionic liquid system†

Wenjing Zhou, [ab] Jianbo Liu, *[ab] Steven D. Chambreau [c] and Ghanshyam L. Vaghjiani [d]

Received 7th June 2024,
Accepted 17th July 2024

DOI: 10.1039/d4cp02329c

rsc.li/pccp

The formation and fragmentation of negatively charged 2-hydroxyethylhydrazinium nitrate ($[HOCH_2CH_2NH_2NH_2]^+NO_3^-$, HEHN) ionic liquid clusters were examined using a guided-ion beam tandem mass spectrometer furnished with collision-induced dissociation of selected ions with Xe atoms. Measurements included the compositions of cluster ions formed in the ionization source, and the dissociation products, cross sections, and 0 K threshold energies for individually selected cluster ions. To identify the structures of the main cluster ion series $[(HEHN)_n(HNO_3)_{0-1}NO_3]^-$ formed, molecular dynamics simulations were employed to create initial geometry guesses, followed by optimization at the ωB97XD/6-31+G(d,p) level of theory, from which global minimum structures were identified for reaction thermodynamics analyses. A comparison was made between the cluster formation and fragmentation in the negatively charged 2-hydroxyethylhydrazinium nitrate with those in the positive mode (reported by W. Zhou *et al.*, *Phys. Chem. Chem. Phys.*, 2023, **25**, 17370). In both modes, the cluster ions were predominantly composed of *m*/*z* below 350; loss of a neutral 2-hydroxyethylhydrazinium nitrate ion pair represents the most important cluster fragmentation pathway, followed by intra-ion pair proton transfer-mediated 2-hydroxyethylhydrazine and HNO_3 elimination; and all clusters started to dissociate at threshold energies less than 1.5 eV. The overwhelming similarities in the formation and fragmentation chemistry of positively *vs.* negatively charged 2-hydroxyethylhydrazinium nitrate clusters may be attributed to their inherent ionic nature and high electric conductivities.

1 Introduction

Ionic liquids (ILs)[1] were first utilized as green solvents for synthesis,[2] catalysis,[2] extraction,[3] and crystallization.[4] The capability and flexibility in designing, tailoring, and customizing IL chemical and physical properties for targeted criteria allow their applications to be extended to more versatile fields, such as additives for enhancing reactivity and durability in fuel cells,[5] electrolytes in lithium-ion batteries,[6] CO_2 capture and utilization,[7] gas sensors,[8] hydraulic oils,[9] ion gels,[10] and alternative energy sources[11–18] for propulsion. These applications are based on the reduced toxicity and lower vapor pressure of ILs, as well as their ionic nature, higher electrical conductivities, and lower viscosities.

The adoption of ILs for various applications has greatly promoted the fundamental research on IL thermochemistry and chemical reactions. Many of these works were accomplished *via* mass spectrometry,[19–28] since mass spectrometry represents a compelling avenue to explore the mechanisms, kinetics, and dynamics for the chemical reactions and fragmentation of single IL constituent ions and ionic clusters, both in the presence and the absence of counter ions.[29] 2-Hydroxyethylhydrazinium nitrate[30] (abbreviated as HEHN, $[HOCH_2CH_2NH_2NH_2]^+NO_3^-$) is a protic IL, produced by the stoichiometric neutralization of 2-hydroxyethylhydrazine (HE) with HNO_3. It is a liquid at ambient temperature with a glass transition temperature of 216.1 K and a melting point of 228 K.[31] There have been multiple mechanistic studies on the thermal and catalytic decomposition of 2-hydroxyethyl-hydrazinium nitrate reported in the literature.[30,32–34] From the perspective of cluster formation,

[a] *Department of Chemistry and Biochemistry, Queens College of the City University of New York, 65-30 Kissena Blvd., Queens, New York 11367, USA. E-mail: jianbo.liu@qc.cuny.edu; Tel: 1-718-997-3271*
[b] *PhD Program in Chemistry, the Graduate Center of the City University of New York, 365 5th Ave., New York, New York 10016, USA*
[c] *Jacobs Technology, Inc., Air Force Research Laboratory, Edwards Air Force Base, California 93524, USA*
[d] *In-Space Propulsion Branch, Rocket Propulsion Division, Aerospace Systems Directorate, Air Force Research Laboratory, AFRL/RQRS, Edwards Air Force Base, California 93524, USA*

† Electronic supplementary information (ESI) available: Conformations and Cartesian coordinates for cluster ions, PES for $[(HEHN)NO_3]^-$, and CID mass spectra for large clusters. See DOI: https://doi.org/10.1039/d4cp02329c

Prince *et al.*[25] measured the first mass spectra for the HEHN cluster ions in 2012 and later simulated dissociation kinetics of $[(HEHN)_{1-3}HE + H]^+$.[35] In 2018, Patrick *et al.*[28] reported collision-induced dissociation (CID) of $[(HE)_2 + H]^+$ and $[(HEHN)_2HE + H]^+$. In 2020, Zeng *et al.*[36] characterized H-bonding motifs in $[(HEHN)_{1-5}HE + H]^+$. More recently, we completed a combined mass spectrometry and dynamics study of the formation and dissociation of $[(HEHN)_n(HE)_{1-2} + H]^+$, $[(HE)_{n+1} + H]^+$, and $[(HE)_nC_2H_4OH]^+$ (n = 0–2).[37] Our work demonstrated the formation of extensive cluster ions[38,39] and nanoclusters,[40] in addition to single ions, and found that the cluster formation is intimately correlated with in- and after-source cluster fragmentation.[28,35,41–49]

In the present work, we have expanded our investigations to the negatively charged clusters of 2-hydroxyethylhydrazinium nitrate. The motivations are rationalized as follows. ILs consist of cationic and anionic components. During the formation of charged clusters in the gas phase, ions and clusters of a single polarity are extracted from ILs. The remaining counterions are accumulated in the liquid, which must be neutralized through electrochemical reactions (otherwise, the extra counterions would build up a field counter to the externally applied ionization field, negatively affecting ion migration in the liquid and ion trajectory in the gas phase[50]). However, electrochemical reactions bring changes in the IL compositions. Alternating the ionization between positive and negative modes can suppress electrochemical reactions.[51,52] The mechanism behind the bipolar mode is that a double layer structure forms at the electrode–liquid interface due to charge transfer between the electrode and emitted ions. As the voltage alternates, the potential difference across the double layer drops and mitigates electrochemical reactions,[51] rendering the possibility of efficient ion formation.

However, there is a dearth of information on negative IL clusters in the literature.[49,53,54] To the best of our knowledge, the present work represents the first paper on the compositions, structures, and reactions of the HEHN clusters in the negative mode. The subsequent sections of this paper are structured as follows. Section 2 provides a concise overview encompassing instrumentation, experimental setup, and data analysis for the measurement of negatively charged ion compositions and kinetic energy-dependent CID of selected cluster ions. Section 3 describes classical molecular dynamics simulations, quasi-classical direct dynamics simulations, and density functional theory (DFT) calculations used in the search for probable cluster structures and dissociation pathways. Section 4 reports the negative mass spectrum of HEHN and the CID of selected primary ions. The negative cluster dissociation behaviors are further discussed and compared to their positive counterparts in Section 5. Conclusions are presented in Section 6.

2 Experimental section

2.1 MS and MS/MS measurements

Mass spectra were measured on a home-built guided-ion beam tandem mass spectrometer located at CUNY Queens College.[55] Here only a concise description is given focusing on the instrumentation parameters used in this study. The mass spectrometer consists of, in a sequential order, a source chamber that was coupled to an ion source, a hexapole radio-frequency (rf) ion guide, a reactant-selection quadrupole mass filter, an octopole ion guide surrounded by a scattering cell, a product-detection mass filter, and a pulse-counting electron multiplier. A 35-gauge hypodermic stainless steel ion emitter (0.13 mm o.d. × 0.05 mm i.d.) was operated at a voltage of −2.0 to −4.0 kV relative to the ground with a flow rate of 0.06 mL hour^{-1}. The HEHN sample was diluted to a concentration of 5 mM. A variety of solvents were tested for negative clusters of HEHN, following the same protocol used for other ILs.[37,56] An acetonitrile : water 3 : 1 solution which had previously been chosen for the positive clusters of HEHN[37] yielded the best stability and ion abundance in the negative mode as well. Acetonitrile also prevented corona discharge at the emitter that otherwise would occur in the ionization of pure aqueous solutions.[56–59] No additional pH adjustment was needed.

The charged liquid droplets emitted from the source underwent desolvation as they passed through a heated inlet capillary (in the temperature range of 120–180 °C, which was biased between −70 and −180 V relative to the ground) and converted into gaseous ions in the source chamber. A skimmer of a 1.0-mm orifice was located at 3 mm away from the end of the capillary. The skimmer was biased at −20 to −60 V relative to the ground. The electrical field between the end of the capillary and skimmer promoted collision induced desolvation of the remaining solvent clusters.[60–62] Ions that passed through the skimmer were transported into the hexapole ion guide for collisional energy damping and space focusing,[63–65] through which ions were thermalized to a Boltzmann internal energy distribution at 310 K[55] and tightly focused into the entrance of the first quadrupole mass filter.

For measurement of primary ion compositions, the first quadrupole mass filter operated in an rf ion-guide mode, and all ions were transmitted to the second quadrupole mass filter for mass scanning. For measurement of CID tandem MS, ions were mass selected in the first quadrupole mass filter. The selected ions were focused into the octopole ion guide that passes through the 10 cm scattering cell wherein the ions underwent CID with the Xe gas (Spectral Gases, 99.95%). The octopole not only trapped ions in the radial direction using an rf potential but also controlled the kinetic energy of ions in the laboratory frame (E_{lab}) using a DC bias. The latter set the collision energy (E_{col}) between the ions and neutral target in the center-of-mass (CM) frame *via* $E_{CM} = E_{lab} \times m_{neutral}/(m_{ion} + m_{neutral})$, where $m_{neutral}$ and m_{ion} indicate the masses of the neutral atom and ion, respectively. The absolute pressure of Xe gas inside the scattering cell was maintained at less than 0.04 mTorr and measured using a capacitance manometer. The low target gas pressure was essential for ensuring, at most, single collisions between ions and the Xe atoms. This simplified data analysis as we only needed to consider energy transfer for single collision events. Under single-collision conditions, the kinetic-energy dependent dissociation cross section (σ) was

determined using a thin-target approximation,[66] *i.e.*, $\sigma = k_B T \cdot \frac{I_{product}}{I_{reactant} \times P_{cell} \times l_{cell}}$, where k_B is the Boltzmann constant, T is the temperature of reactants, P_{cell} is the target gas pressure in the scattering cell, l_{cell} is the effective cell length, and $I_{reactant}$ and $I_{product}$ are the intensities of reactant ions (when the Xe gas was not directed into the scattering cell) and product ions (after correcting for the background when Xe was no longer directed into the cell), respectively. The experiment was repeated four times under the same conditions, from which relative uncertainties were determined.

2.2 Analysis of 0 K dissociation threshold energy (E_0)

E_0 was determined from E_{CM}-dependent product ion cross sections following a line-of-centers (LOC) model-based analysis:[67–70]

$$\sigma\,(E_{CM}) = \sigma_0 \frac{(E_{CM} + E_{vib} + E_{rot} - E_0)^n}{E_{col}} \quad (1)$$

where σ_0 is a normalization factor, E_{CM} and E_0 are as described before, E_{vib} and E_{rot} are the vibrational and rotational energies of reactant ions, and n is a fitting parameter that determines the energy transfer efficiency from E_{CM} to E_{vib} and E_{rot}. The hypothesis behind the LOC model is that a fraction of near-threshold collisions are completely inelastic so that all E_{CM} contributes to overcome E_0, as previously verified in the threshold CID of various ionic species[69–71] including IL cluster ions.[37,56]

The energy dependence of experimental $\sigma(E_{CM})$ was broadened by the translational energy distributions of primary ions and target gas and the internal energy distributions of primary ions.[72,73] A Monte Carlo program was used to simulate the experimental energy broadening, including convolution and fitting.[74,75] In brief, for each product ion channel at each nominal E_{CM}, the simulation initiated a set of 100 000 ions with Boltzmann distributions of E_{vib} and E_{rot} at the experimental ion temperature 310 K. Each ion had a translational kinetic energy drawn from a Lorentzian distribution of E_{lab}. The Lorentzian distribution had a peak value corresponding to the desired E_{CM} and the full-width at half maximum (fwhm, representing the ion kinetic energy width) of 0.65 eV as determined by a retarding potential scan on the octopole.[55,76] The thermal motion for the Xe atoms sampled the translational energy distribution at room temperature. To take into account the kinetic shift[77] in near-threshold collisions, a Rice–Ramsperger–Kassel–Marcus (RRKM) unimolecular rate model[78] was incorporated into the fitting to calculate dissociation rates with total available energies. Only the collisions that had led to a dissociation within the ion time-of-flight (100 to 500 μs depending on E_{CM}) were counted toward $\sigma(E_{CM})$. The collision outcomes at various E_{CM} were fed into eqn (1). A leveling-off function was used to allow $\sigma(E_{CM})$ to reach a plateau at high energies.

3 Computational section

3.1 Classical molecular dynamics simulations of ion conformations followed by DFT calculations

Initial guesses for the conformations of cluster ions were created by classical molecular dynamics simulations using GROMACS.[79,80] The detailed procedure was described previously.[37] As the neutral pair of HE·HNO_3 does not exist within HEHN cluster ions,[28,36,37] only $[HE + H]^+$, NO_3^-, and HNO_3 were fed into the simulations as starting constituents. A space of 3 nm × 3 nm × 3 nm was chosen for simulating cluster ions of $m/z \leq 400$, and that of 4 nm × 4 nm × 4 nm was chosen for larger ions. Hessian matrices for the constituents were derived from Gaussian 16[81] electronic structure calculations. The universal force field and topology files were generated using the Sobtop program.[82] An initial energy-minimization process was carried out under NVT (canonical ensemble of constant temperature and volume). The identified minimum-energy structure served as the starting point in a series of simulated annealing[83] as follows: the simulation ramped the system temperature from 300 K to 500 K within 3 ps, followed by 4 ps at 500 K for dynamics, and another 3 ps for cooling to 300 K. The resulting candidate structure was used as a starting structure to initiate a new annealing iteration.

Following this sequence, a set of 100–200 candidate structures was created to cover most of the probable conformations for each cluster composition. Their geometries were viewed using the VMD program[84] to remove obvious duplicates. All unique structures were optimized using the ωB97XD functional at several basis sets of increasing size. To remove extremely high-energy conformers, we first used a relatively small basis set 3-21G to identify all the conformers (approximately 50) within a 0.8 eV energy range. These conformers were refined by employing the 6-31G(d) basis set, followed by the 6-31+G(d,p) basis set. The DFT calculations also provided harmonic frequencies to distinguish stationary *vs.* saddle points, from which low-energy stable structures and global minima were located.

3.2 Validation of ion conformations using quasi-classical, direct dynamics simulations

As a cross-validation of the classical dynamics simulations, the $[(HEHN)NO_3]^-$ cluster was subjected to Born–Oppenheimer direct dynamics trajectory simulations.[85–89] The trajectories followed the formation of $[(HEHN)NO_3]^-$ *via* collisions of HEHN and NO_3^-. Initial conditions for bimolecular collisions were set up using the Venus program[90,91] coupled to Gaussian. The potential minima of HEHN (*i.e.*, the neutral pair HE·HNO_3) and NO_3^- were calculated at the ωB97XD/6-31+G(d) level of theory. E_{vib} for the normal mode of reactant vibration was selected from a 310 K quantum Boltzmann probability distribution[92] $P(n_i) = \exp(-n_i h\upsilon_i/k_B T)[1 - \exp(-h\upsilon_i/k_B T)]$ where ν_i and n_i are the vibrational frequency and quantum number of the ith mode, respectively; and T is the temperature of the reactant. The resulting normal mode energy, including zero-point energy (ZPE), was partitioned between kinetic and

potential energies by choosing a random phase for each mode. The E_{rot} of the reactants was sampled from a classical Boltzmann distribution at 310 K. E_{vib} and E_{rot} were transferred into reactant momenta and displacements from equilibrium Cartesian coordinates. Reactants were randomly rotated about their Euler angles. Relative velocities were added to reactants in accord with E_{CM}.

Trajectories started at an initial center-of-mass distance of 8.0 Å and halted after the formation of a cluster ion or when product separation exceeded 10.0 Å. The E_{CM} (0.5 eV) was low enough to allow for complex formation in collisions, but it was not so low as to substantially increase the trajectory integration time. The impact parameters (b) was chosen randomly between 0 and b_{max} (4.5 Å, estimated from the maximum collision cross section using the IMoS program[93,94]). The on-the-fly energies and gradients were calculated using the Hessian-based predictor–corrector integration algorithms[88] implemented in the Gaussian software, with Hessians updated every five steps. The ωB97XD/6-31+G(d) level of theory was chosen for the integration as it represents a good compromise between accuracy and computational cost for IL dynamics.[37,56,95–97] The trajectory propagation step size was set at 0.25 amu$^{1/2}$ Bohr (equivalent to a step size of 0.4 fs in trajectory time) to ensure the conservation of energy and momentum.

3.3 DFT calculation of dissociation energies

Geometry optimization and energy calculations for the reactants and fragments were conducted at the ωB97XD/6-31+G(d,p) level of theory using Gaussian 16. Their Cartesian coordinates are provided in the ESI.† Cluster ion dissociation enthalpies were calculated at 0 K and have taken into account ZPEs (scaled by a factor of 0.975)[98] to allow for a direct comparison with the CID experimental data. Reaction potential energy surfaces (PESs) were calculated at 298 K.

4 Results

4.1 Formation of HEHN cluster ions in the negative mode

A mass spectrum of the negatively charged HEHN cluster ions is depicted in Fig. 1. For visual clarity, ion intensities in the m/z range above 700 are scaled by a factor of 10 and presented in blue; however, the portion of these ions accounts for only 4% of the total ions detected in the experiment. Most of the species can be grouped into three distinct series: $[(HEHN)_nNO_3]^-$ (n = 0–13), $[(HEHN)_n(HNO_3)NO_3]^-$ (n = 0–2), and $[(HEHN)_n(NaNO_3)NO_3]^-$ (n = 0–10). Each series is associated with the progression of HEHN. Out of the three series, $[(HEHN)_nNO_3]^-$ represents the dominating one and presents the longest progression; but the intensity decays exponentially from n = 1 to 5, becoming insignificant afterwards. $[(HEHN)_n(HNO_3)NO_3]^-$ represents the second most important series, albeit the progression lasts only to n = 2. The assignment of the minor series $[(HEHN)_n(NaNO_3)NO_3]^-$ was supported by the CID of $[(NaNO_3)NO_3]^-$ (m/z of 147), which yielded only NO_3^- + $NaNO_3$. Na^+ was also detected in the positive charged HEHN clusters by our group[37] and others,[25] despite the source remaining unknown.

Interestingly, we observed a group of species corresponding to a neutral mass loss of 15 from each cluster ion in the three major series. These species are indicated by asterisks next to their parent ions. The total fragment population is 5.5% in the series of $[(HEHN)_nNO_3]^-$ and in the series of $[(HEHN)_n(HNO_3)NO_3]^-$, and increases to 16.5% in the series of $[(HEHN)_n(NaNO_3)NO_3]^-$. The same mass 15 elimination was reported by Chambreau and co-workers previously.[34] While they attributed

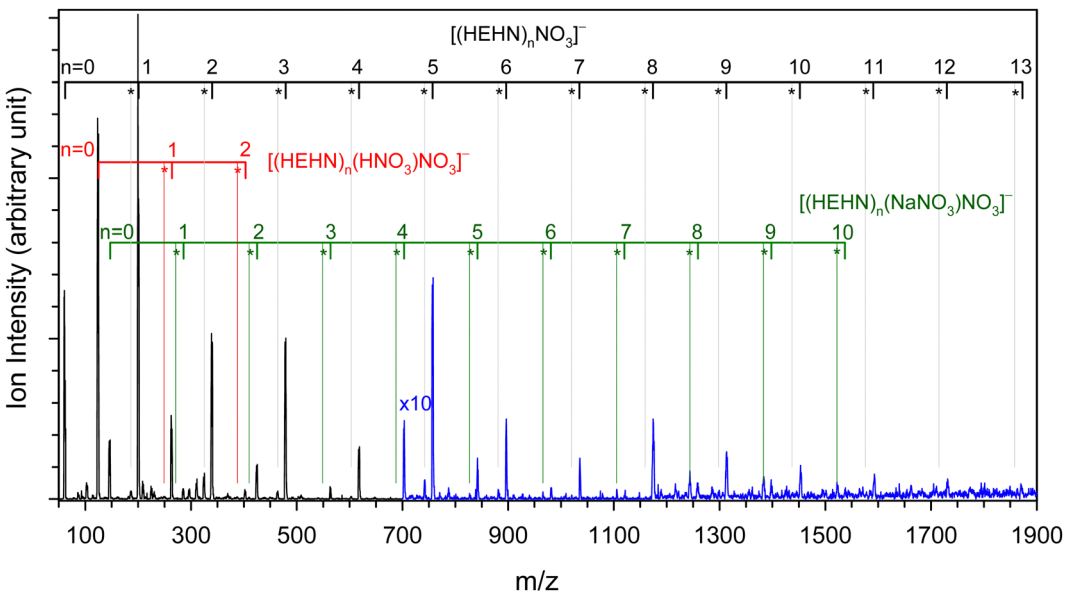

Fig. 1 Formation of negatively charged HEHN cluster ions when using 5 mM HEHN in acetonitrile/water (3 : 1). Ion intensities of m/z > 700 are scaled by a factor of 10.

the neutral fragment to a $^{\bullet}CH_3$ radical, NH represents another possibility. The DFT-calculated activation barrier for NH-elimination in HEHN is 4.52 eV. The elimination leads to a product-like complex first, which ultimately dissociates to $HOCH_2CH_2NH_2$ + NH at 4.73 eV. The acquisition of these amounts of activation and dissociation energies was possible upon in-source collisional activation (*i.e.*, within the electric field between the end of the capillary and skimmer). Note the $[(HEHN)_n(NaNO_3)NO_3]^-$ series has a higher NH-elimination probability than $[(HEHN)_nNO_3]^-$, which implies that the clusters containing $NaNO_3$ weaken intra-cluster interaction. Also note that the in-source dissociation was observed in the positively charged HEHN clusters previously.[37] In the latter case, the dissociation was mediated by N_2H_4 elimination from a $[HE + H]^+$ moiety, producing $[(HE)_nC_2H_4OH]^+$ fragments in the $[(HE)_{n+1} + H]^+$ series.

4.2 Dissociation of $[(HEHN)_nNO_3]^-$

$[(HEHN)NO_3]^-$ (*m*/*z* 201). This ion not only represents the lightest HEHN cluster but also accounts for 26% of the total ion population in the negatively charged clusters. A tandem CID product ion mass spectrum of $[(HEHN)NO_3]^-$, recorded at E_{CM} = 3 eV, is presented in Fig. 2a. Product ions include $[(HE)NO_3]^-$ at *m*/*z* 138 (which corresponds to HNO_3 elimination), $[(HNO_3)NO_3]^-$ at *m*/*z* 125 (corresponding to HE elimination), and NO_3^- at *m*/*z* 62 (corresponding to HEHN elimination).

Prior to the investigation of cluster dissociation mechanisms, GROMACS-based classical dynamics simulations were conducted to explore the probable conformations of $[(HEHN)NO_3]^-$. In this pursuit, 100 candidate geometries were generated for optimization at the ωB97XD level using the 3-21G basis set. Geometries of low-energy conformations were re-optimized using 6-31G(d) and then 6-31+G(d,p). Nine different conformations were identified within the energy range of 0.06 eV, as presented in the order of relative enthalpy in Fig. S1 in the ESI.† In parallel, Venus-based direct dynamics simulations were executed to follow the reaction of HEHN + NO_3^- at the collision energy of 0.5 eV. Due to the extensive trajectory computing time (on average each trajectory took 240 CPU hours), we accumulated only 100 trajectories, most of which led to a complex. These complex structures were subjected to geometry optimization at the ωB97XD/6-31+G(d,p) level of theory. Remarkably, the Venus results were able to duplicate five conformations in Fig. S1 (ESI†), *i.e.*, $[(HEHN)NO_3]^-$_a, c, e, g and h, and predicted the same global minimum conformation as GROMACS.

The two lowest-energy conformers, $[(HEHN)NO_3]^-$_a and b, differ in energy by less than 0.001 eV. The combination of the two accounts for a thermal Boltzmann population of 68%. They were used as the starting reactants in calculating the dissociation enthalpies for reactions (2b)–(2d).

$$[(HEHN)NO_3]^- \rightarrow [(HE)NO_3]^- + HNO_3 \quad \Delta H\ (0\ K) = 1.63\ eV \quad (2b)$$

$$\rightarrow [(HNO_3)NO_3]^- + HE \quad \Delta H\ (0\ K) = 1.20\ eV \quad (2c)$$

$$\rightarrow NO_3^- + HEHN \quad \Delta H\ (0\ K) = 1.80\ eV \quad (2d.1)$$

$$\rightarrow NO_3^- + HE + HNO_3 \quad \Delta H\ (0\ K) = 2.59\ eV \quad (2d.2)$$

To probe the evolution of the HEHN moiety structure as well as the mechanisms for HE and HNO_3 elimination in $[(HEHN)NO_3]^-$, a static PES scan (without adding kinetic

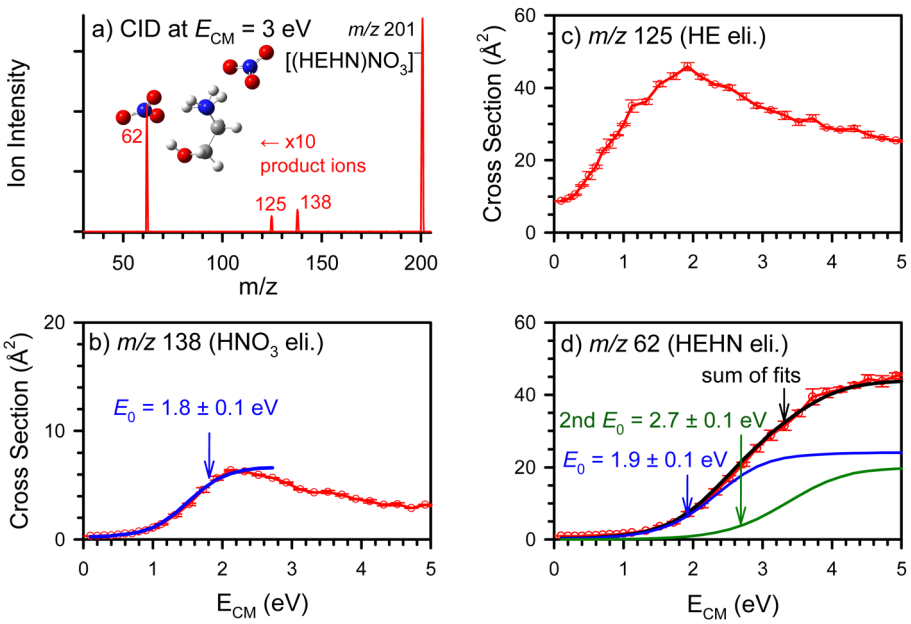

Fig. 2 (a) Structure and a representative CID product ion mass spectrum for $[(HEHN)NO_3]^-$, wherein the product ion intensities are scaled by a factor of 10; and (b)–(d) individual product ion cross sections as a function of E_{CM}, wherein the red lines with error bars represent the experimental data and the blue, green, and black lines represent the LOC fits.

energy) was carried out along the center-of-mass separation between HEHN and NO_3^- using the ωB97XD/6-31G+(d,p) method. The PES is plotted in Fig. S2 in the ESI,† along with the changes of two H-bonds $r(HE\cdots H^+)$ and $r(H^+\cdots NO_3^-)$. As shown in Fig. S2a (ESI†), the HEHN moiety adopts an ion-pair structure within the cluster and remains ionic in nature during the elimination of extra NO_3^-. However, it has the possibility of transitioning to a H-bonded neutral pair at the product asymptote, as one may expect from the trends of change in $r(HE\cdots H^+)$ and $r(H^+\cdots NO_3^-)$. Furthermore, the activation barrier for reverse proton transfer (PT) within a single HEHN is only 0.02 eV – which can be easily overcome by collisional activation. In other words, there may exist a collisionally activated, product-like complex $[(HE)(HNO_3)NO_3]^-$. The fact that both HE and HNO_3 elimination was observed supports this hypothesis.

At E_{CM} below 3.0 eV, HE elimination represents the dominant dissociation mechanism for $[(HEHN)NO_3]^-$. The 0 K dissociation threshold for HE elimination is relatively low (1.20 eV), resulting in a non-zero cross section at the lowest experimental energy due to reactants internal energy and translational kinetic energy spread and Doppler broadening. For this reason, LOC fitting for the HE elimination cross sections was not feasible (the same reason applies to the product channels for other clusters which have non-zero cross sections at the lowest E_{CM}). The HNO_3 elimination cross section, on the other hand, declines (rather than levels off) at high energies. We attempted to fit the HNO_3 elimination only in the E_{CM} range of 0.05–2.7 eV. The testing fit allowed us to estimate an E_0 of 1.8 eV, close to the calculated ΔH (0 K) of 1.63 eV.

There are noticeable decreases in the cross sections for both HNO_3 and HE elimination at E_{CM} above 2.0 eV. These are due to the competition with HEHN elimination at higher energies, as is evidenced by the fact that the sum of all product ion cross sections at high E_{CM} equals to the collision cross section of $[(HEHN)NO_3]^-$ + Xe. The question arises as to whether the HEHN elimination was due to reaction (2d.1) or (2d.2), or their combination. We first found that no satisfactory LOC fit could be obtained for the HEHN elimination cross section (Fig. 2d) using a single $\sigma(E_{CM})$ function. We therefore fitted the cross section using two sets of $\sigma(E_{CM})$ functions. E_0, n, and leveling off energy for each set were adjusted independently to reach the best fit for the cross section. As illustrated by the blue and green curves in Fig. 2d, the first LOC fit has E_0 = 1.9 eV, n = 2.4, and leveling off energy of 3.4 eV, and the second fit has E_0 = 2.7 eV, n = 2.3, and leveling off energy of 4.6 eV. The black curve represents the sum of the two fits. The results of LOC fitting have reinforced our hypothesis that there exist two cluster structures upon collisional activation and therefore two dissociation pathways. By comparing to the calculated ΔH (0 K), we conclude that the low-threshold, single HEHN elimination (*i.e.*, reaction (2d.1)) dominates throughout the entire energy range, while the high-threshold, concomitant elimination of (HE + HNO_3) (*i.e.*, reaction (2d.2)) becomes important only at high energies. Our results reflect the reliability and robustness of the threshold CID and the LOC simulation for dissociation energies.[99] As we may infer from the LOC fits in Fig. 2d, the ratio of activated $[(HEH^+NO_3^-)NO_3]^-$ to $[(HE)(HNO_3)NO_3]^-$ is 5 : 4 at high energies.

$[(HEHN)_2NO_3]^-$ (m/z 340). The dissociation of $[(HEHN)_2NO_3]^-$ (Fig. 3a) resembles that of $[(HEHN)NO_3]^-$ in terms of HE and HEHN elimination. The new features include elimination of 2HE, 2HEHN, and HEHN + HE; on the other hand, no single HNO_3 elimination was observed.

The combined approach of GROMACS classical dynamics simulations and DFT geometry optimization was used to determine explicit cluster structures for $[(HEHN)_2NO_3]^-$. Four stable conformations were identified within an energy range of 0.12 eV (see Fig. S3 in the ESI†). The global-minimum conformer constitutes 82% of the thermal population and was selected as the reactant structure to calculate the following dissociation enthalpies.

$$[(HEHN)_2NO_3]^-$$

$$\rightarrow [(HEHN)(HNO_3)NO_3]^- + HE \quad \Delta H\ (0\ K) = 1.33\ eV \quad (3b)$$

$$\rightarrow [(HEHN)NO_3]^- + HEHN \quad \Delta H\ (0\ K) = 1.47\ eV \quad (3c.1)$$

$$\rightarrow [(HEHN)NO_3]^- + HE + HNO_3 \quad \Delta H\ (0\ K) = 2.26\ eV \quad (3c.2)$$

$$\rightarrow [(HNO_3)_2NO_3]^- + 2HE \quad \Delta H\ (0\ K) = 2.57\ eV \quad (3d)$$

$$\rightarrow [(HNO_3)NO_3]^- + HEHN + HE \quad \Delta H\ (0\ K) = 2.67\ eV \quad (3e)$$

$$\rightarrow NO_3^- + (HEHN)_2 \quad \Delta H\ (0\ K) = 2.04\ eV \quad (3f.1)$$

$$\rightarrow NO_3^- + 2HEHN \quad \Delta H\ (0\ K) = 3.27\ eV \quad (3f.2)$$

$$\rightarrow NO_3^- + HEHN + HE + HNO_3 \quad \Delta H\ (0\ K) = 4.06\ eV \quad (3f.3)$$

$$\rightarrow NO_3^- + 2HE + 2HNO_3 \quad \Delta H\ (0\ K) = 4.84\ eV \quad (3f.4)$$

Since the cross sections for single HE and HEHN elimination (Fig. 3b and c) exceed zero at the lowest E_{CM}, LOC fitting of their threshold profiles was not feasible. As aforementioned, there are two possible pathways leading to HEHN elimination: either elimination of a single HEHN (*i.e.*, neutral pair evaporation[46]) as specified by reaction (3c.1) or concomitant elimination of separated HE + HNO_3 as specified by reaction (3c.2). However, reaction (3c.2) has a ΔH (0 K) at 2.26 eV, which is inconsistent with the downward inflection for product ions m/z 201 around 1.6 eV and therefore could be ruled out.

On the other hand, the LOC fitting was able to reproduce the cross sections for 2HE, (HEHN + HE), and 2HEHN elimination (Fig. 3d–f) over two orders of magnitude and from an energy below the threshold to 7 eV, except for the decay in 2HE elimination at $E_{CM} > 3.6$ eV. The fitted experimental E_0 values have not only reached an excellent match with the calculated ΔH (0 K) for reactions (3d) and (3e), but also determined the most probable pathway leading to NO_3^- (m/z 62). Among the four proposed product channels (3f.1)–(3f.4), the last two could be ruled out because both would require the experimentally excluded, single or double HNO_3 elimination. Reaction (3f.1) presents elimination of dimeric $(HEHN)_2$ with ΔH (0 K) at 2.04 eV; however, the corresponding low ΔH (0 K) does not fit to the relatively high-threshold profile in Fig. 3f. Consequently,

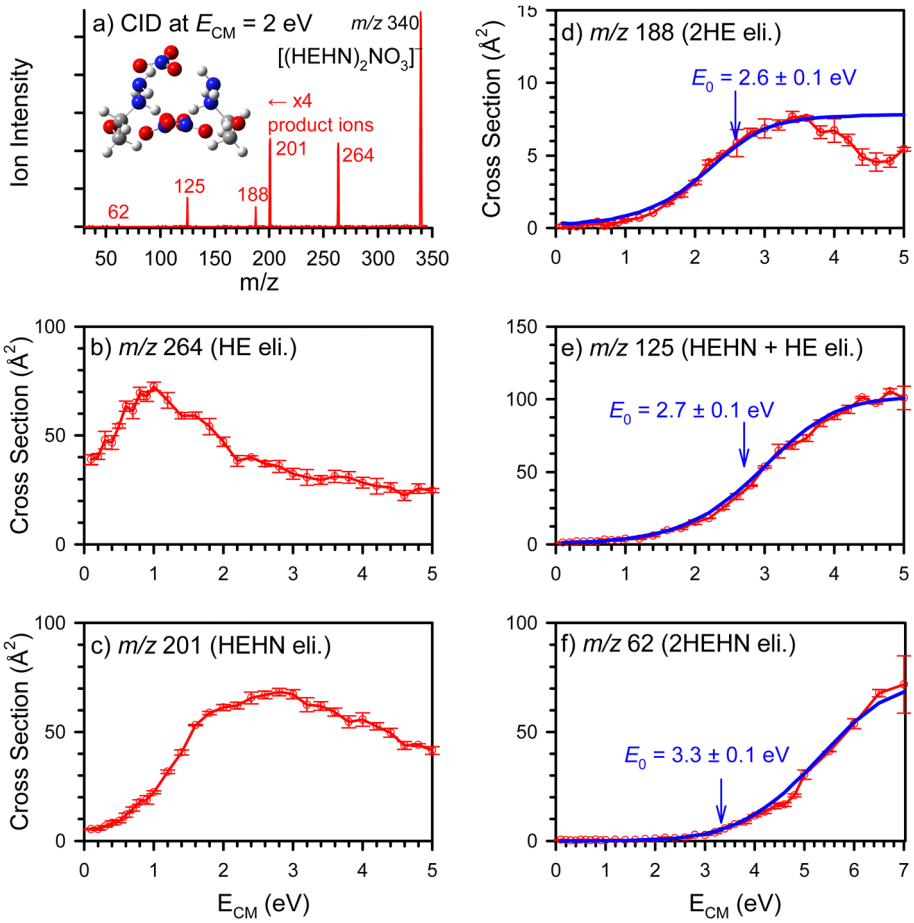

Fig. 3 (a) Structure and a representative CID product ion mass spectrum for $[(HEHN)_2NO_3]^-$, wherein the product ion intensities are scaled by a factor of 4; and (b)–(f) individual product ion cross sections as a function of E_{CM}, wherein the red lines with error bars represent the experimental data and the blue lines represent the LOC fits.

reaction (3f.2) is the only possibility. The LOC fitted E_0 (3.3 eV) perfectly matches the calculated ΔH (0 K, 3.27 eV) for reaction (3f.2), indicating that this identification is unambiguous.

$[(HEHN)_3NO_3]^-$ (*m*/*z* 479). The CID results for $[(HEHN)_3NO_3]^-$, as well as the LOC fits to the applicable product channels, are summarized in Fig. 4. Probable conformations of $[(HEHN)_3NO_3]^-$ are provided in Fig. S4 in the ESI.† The fragmentation of $[(HEHN)_3NO_3]^-$ follows a similar pattern as $[(HEHN)_2NO_3]^-$, including elimination of multiple HE and HEHN. But elimination of single HNO_3 was not observed.

Using the lowest-energy and population-dominating (92%) conformer (*i.e.*, $[(HEHN)_3NO_3]^-$_a in Fig. S4, ESI†) as the starting reactant, the dissociation enthalpies for various pathways were calculated as follows:

$[(HEHN)_3NO_3]^-$

$\rightarrow [(HEHN)_2(HNO_3)NO_3]^- + HE \quad \Delta H\ (0\ K) = 1.44\ eV$ (4b)

$\rightarrow [(HEHN)_2NO_3]^- + HEHN \quad \Delta H\ (0\ K) = 1.40\ eV$ (4c)

$\rightarrow [(HEHN)(HNO_3)_2NO_3]^- + 2HE \quad \Delta H\ (0\ K) = 2.76\ eV$ (4d)

$\rightarrow [(HEHN)(HNO_3)NO_3]^- + HEHN + HE \quad \Delta H\ (0\ K) = 2.73\ eV$ (4e)

$\rightarrow [(HEHN)NO_3]^- + (HEHN)_2 \quad \Delta H\ (0\ K) = 1.65\ eV$ (4f.1)

$\rightarrow [(HEHN)NO_3]^- + 2HEHN \quad \Delta H\ (0\ K) = 2.87\ eV$ (4f.2)

$\rightarrow [(HEHN)NO_3]^- + HEHN + HE + HNO_3 \quad \Delta H\ (0\ K) = 3.66\ eV$ (4f.3)

$\rightarrow [(HNO_3)NO_3]^- + 2HEHN + HE \quad \Delta H\ (0\ K) = 4.07\ eV$ (4g.1)

$\rightarrow [(HNO_3)NO_3]^- + HEHN + 2HE + HNO_3 \quad \Delta H\ (0\ K) = 4.85\ eV$ (4g.2)

The significant cross sections for the HE elimination and HEHN elimination at the lowest experimental energy align with the relatively low ΔH (0 K) calculated for reactions (4b) and (4c). The two cross sections decrease dramatically at high energies due to the increasing elimination of (HEHN + HE), reaction (4e). It is interesting to note that elimination of 2HE, reaction (4d), has an extremely low cross section (Fig. 4d). The same phenomenon was observed in the dissociation of $[(HEHN)_2NO_3]^-$. The implication is that the clusters have difficulty in accommodating reverse PT in more than one HEHN moiety. The LOC fitting has reproduced the cross sections in Fig. 4e and f, and the resulting E_0 values agree well with the DFT calculated ΔH (0 K). Similar to

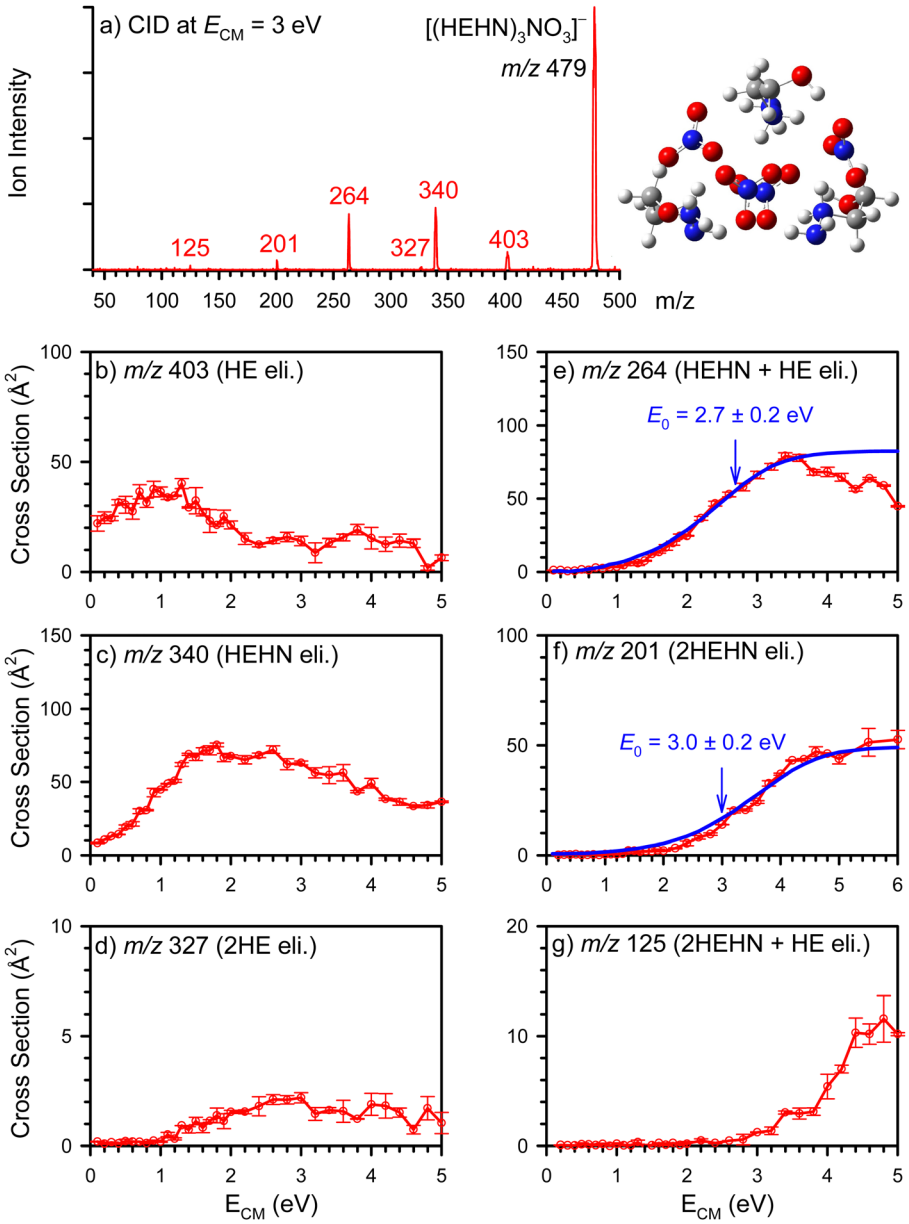

Fig. 4 (a) Structure and a representative CID product ion mass spectrum for $[(HEHN)_3NO_3]^-$; and (b)–(g) individual product ion cross sections as a function of E_{CM}, wherein the red lines with error bars represent the experimental data and the blue lines represent the LOC fit.

the scenario for $[(HEHN)_2NO_3]^-$, the LOC fitting identified reaction (4f.2) as the most probable mechanism for simultaneous 2HEHN elimination.

$[(HEHN)_{4-10}NO_3]^-$ (*m/z* 618, 757, 896, 1035, 1174, 1313, 1452). Fig. S5–S7 in the ESI,† provide the CID results for each of $[(HEHN)_{4-6}NO_3]^-$. Because of the large cluster sizes, it became difficult to calculate their probable conformations and identify dominating ones. Similar to their low-mass analogues in the series, the CID of $[(HEHN)_{4-6}NO_3]^-$ is dominated by elimination of a single HEHN at the low energy range (2–3 eV), which is outcompeted by elimination of simultaneous 2HEHN at the medium energy range (4–6 eV) and by elimination of (2HEHN + HE) and/or 3HEHN at the high energy range. Across the entire energy range, HE elimination remains minor. This is the case when HE appears either as the only neutral fragment or accompanied by the HEHN loss. It implies that reverse PT becomes increasingly difficult in large cluster ions where each HEHN ion pair is surrounded by or encapsulated within other ion pairs.

Due to the significantly low intensities of the $[(HEHN)_{7-10}NO_3]^-$ cluster ions (less than 100 counts s^{-1}), we were able to only measure their dissociation product ions (as depicted in Fig. S8 in the ESI†) but not cross sections. Their major dissociation pathway corresponds to the elimination of a single HEHN. The second major pathway leads to HE loss. The elimination of 2–3 HEHN moieties was also observed.

4.3 Dissociation of $[(HEHN)_n(HNO_3)NO_3]^-$

$[(HNO_3)NO_3]^-$ (m/z 125). This species "does not belong" to the HEHN clusters; nevertheless, both $[(HNO_3)NO_3]^-$ and NO_3^- together accounts for one third of the total negative ions. The CID of $[(HNO_3)NO_3]^-$ in Fig. 5 presents only the elimination of HNO_3. The LOC-fitted E_0 is close to the calculated ΔH (0 K) for reaction (5).

$$[(HNO_3)NO_3]^- \rightarrow HNO_3 + NO_3^- \quad \Delta H\ (0\ K) = 1.38\ eV \tag{5}$$

$[(HEHN)_{1-2}(HNO_3)NO_3]^-$ (m/z 264 and 403). The probable conformations for these two clusters are provided in Fig. S9 and S10 in the ESI.† For $[(HEHN)(HNO_3)NO_3]^-$, the lowest-energy conformer represents a Boltzmann equilibrium population of 45%, while all the others have populations ranging from a few percentage points to 22%. For $[(HEHN)_2(HNO_3)NO_3]^-$, the lowest-energy conformer represents a Boltzmann equilibrium population of 75%. Therefore, their global-minimum conformations were used as the initial structures for thermochemistry calculations. The fragmentation pathways for $[(HEHN)(HNO_3)NO_3]^-$ and $[(HEHN)_2(HNO_3)NO_3]^-$ include the loss of HNO_3, HE (minor, only in $[(HEHN)(HNO_3)NO_3]^-$), HEHN and HEHN + HNO_3, as shown in Fig. 6 and Fig. S11 in the ESI,† respectively.

Their calculated dissociation enthalpies are as follows, wherein the values in parentheses refer to the reactions of $[(HEHN)_2(HNO_3)NO_3]^-$:

$$[(HEHN)_{1(2)}(HNO_3)NO_3]^- \rightarrow [(HEHN)_{1(2)}NO_3]^- + HNO_3 \quad \Delta H\ (0\ K) = 0.92\ (0.75)\ eV \tag{6b}$$

$$\rightarrow [(HEHN)_{0(1)}(HNO_3)_2NO_3]^- + HE \quad \Delta H\ (0\ K) = 1.24\ (1.33)\ eV \tag{6c}$$

$$\rightarrow [(HEHN)_{0(1)}(HNO_3)NO_3]^- + HEHN \quad \Delta H\ (0\ K) = 1.33\ (1.30)\ eV \tag{6d.1}$$

$$\rightarrow [(HEHN)_{0(1)}(HNO_3)NO_3]^- + HE + HNO_3 \quad \Delta H\ (0\ K) = 2.12\ (2.08)\ eV \tag{6d.2}$$

$$\rightarrow [(HEHN)_{0(1)}NO_3]^- + HEHN + HNO_3 \quad \Delta H\ (0\ K) = 2.72\ (2.22)\ eV \tag{6e.1}$$

$$\rightarrow [(HEHN)_{0(1)}NO_3]^- + HE + 2HNO_3 \quad \Delta H\ (0\ K) = 3.51\ (3.01)\ eV \tag{6e.2}$$

Since the intensity of $[(HEHN)_2(HNO_3)NO_3]^-$ was too low to allow for the measurement of individual product ion cross sections, the CID of $[(HEHN)(HNO_3)NO_3]^-$ in Fig. 6 was used to demonstrate their dissociation energy dependence. There appear to be good agreements between the calculated dissociation enthalpies and experimental cross sections. The cross sections for HE and HNO_3 eliminations drop before reaching their calculated thresholds, indicating that HE and HNO_3 eliminations become less competitive at $E_{CM} \geq 2$ eV. The best LOC fitting of the product ions m/z 125 revealed two product channels, *i.e.*, reactions (6d.1) and (6d.2) with a ratio of 5 : 4 at high energies. The fitting of product ions m/z 62 identified reaction (6e.1) as the most probable mechanism.

5 Discussion

5.1 Ion compositions of different polarities

It is informative to examine and compare ion compositions in different charge modes. Positive clusters of HEHN were reported by Prince *et al.* using field evaporation of pure HEHN from an externally wetted titanium emitter[25] and by our lab using 5 mM HEHN in acetonitrile/water through a stainless steel capillary emitter.[37] Nearly identical cluster ion compositions and intensity distributions were observed in the two different studies. The series of positive clusters of HEHN is dominated by, in the order of importance, $[(HE)_{1-3} + H]^+$, $[(HEHN)_{1-2}HE + H]^+$, $[(HEHN)_{1-2}(HE)_2 + H]^+$, and $[(HE)_{0-2}C_2H_4OH]^+$ (where $C_2H_4OH^+$ was produced by dissociation of HEHN at the C–N bond).[25,37]

Table 1 has compiled cluster ion populations detected in our positive and negative mass spectra. Groups of positive cluster ions are listed side by side with their counterparts in the negative mode. Overall, positive and negative cluster ions present well correlated compositions, such as $[HE + H]^+$ *vs.* NO_3^-, $[(HE)_2 + H]^+$ *vs.* $[H(NO_3)_2]^-$, $[(HEHN)_{1-2}HE + H]^+$ *vs.*

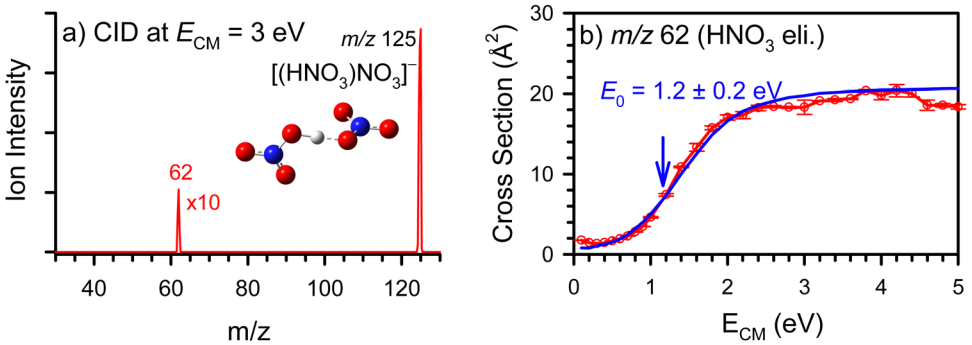

Fig. 5 (a) Structure and a representative CID product ion mass spectrum for $[(HNO_3)NO_3]^-$, wherein the product ion intensity is scaled by a factor of 10; and (b) the product ion cross section as a function of E_{CM}, wherein the red line with error bars represents the experimental data and the blue line represents the LOC fit.

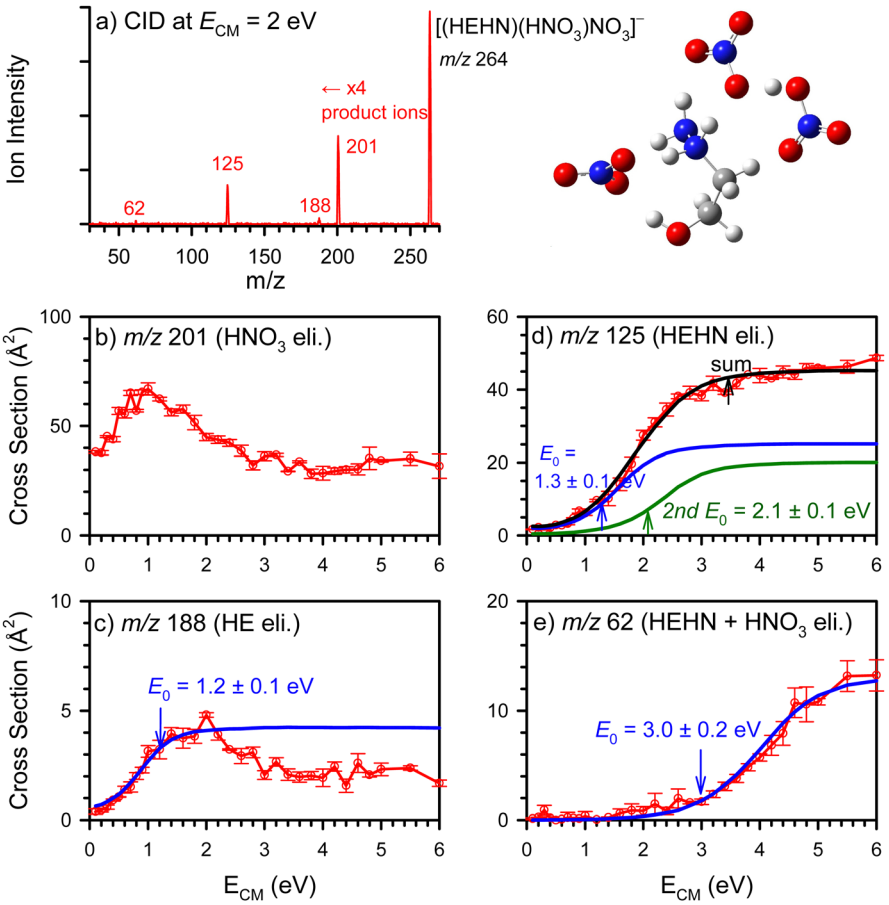

Fig. 6 (a) Structure and a representative CID product ion mass spectrum for $[(HEHN)(HNO_3)NO_3]^-$, wherein product ion intensities are scaled by a factor of 4; and (b)–(e) individual product ion cross sections as a function of E_{CM}, wherein red lines with error bars represent the experimental data and blue, green and black lines represent the LOC fits.

Table 1 Cluster ion compositions in positive *vs.* negative ion modes

Positive clusters[37]	(*m*/*z*)	Ratio%	Negative clusters	(*m*/*z*)	Ratio%
$[HE + H]^+$	(77)	44.8	NO_3^-	(62)	11.3
$C_2H_4OH^+$ (= $[HE + H]^+ - N_2H_4$)	(45)	0.4			
$[HE + H]^+ - H_2O$	(59)	7.0			
$[(HE)Na]^+$		0.7			
$[(HE)_2Na]^+$		1.3	$[Na(NO_3)_2]^-$		3.4
$[(HE)_2 + H]^+$					
$[(HE)C_2H_4OH]^+$	(153)	27.6	$[(HNO_3)NO_3]^-$	(125)	20.7
	(121)	2.0			
$[(HE)_3 + H]^+$	(229)	1.5			
$[(HEHN)HE + H]^+$	(216)	4.0	$[(HEHN)NO_3]^-$	(201)	26.3
$[(HEHN)_2HE + H]^+$	(355)	8.5	$[(HEHN)_2NO_3]^-$	(340)	10.5
			$[(HEHN)_3NO_3]^-$		9.0
			$[(HEHN)_{4-12}NO_3]^-$		5.9
$[(HEHN)(HE)_2 + H]^+$		1.3	$[(HEHN)(HNO_3)NO_3]^-$		4.6
$[(HEHN)_2(HE)_2 + H]^+$		0.9	$[(HEHN)_2(HNO_3)NO_3]^-$		0.5
			$[(HEHN)_{1-9}(NaNO_3)NO_3]^-$		3.7
			Others		4.1

$[(HEHN)_{1-2}NO_3]^-$, and $[(HEHN)_{1-2}(HE)_2 + H]^+$ *vs.* $[(HEHN)_{1-2}(HNO_3)NO_3]^-$. In terms of cluster *m*/*z* distributions, 99% of the positive ions are populated within a *m*/*z* range 40–355 while 80% of the negative ions are populated within *m*/*z* 62–340.

Structurally, positive cluster ions are dominated by $[HE + H]^+$ (and its derivatives, total 53%) and the short progressions of $[(HEHN)_{1-2}HE + H]^+$ (12.5%) and $[(HEHN)_{1-2}(HE)_2 + H]^+$ (2.2%); negative ions are featured by the long progressions of

$[(HEHN)_{1-12}NO_3]^-$ (51.7%), in addition to NO_3^- (11.3%), $[H(NO_3)_2]^-$ (26.3)% and $[(HEHN)_{1-2}(HNO_3)NO_3]^-$ (5.1%).

5.2 Fragmentation pathways and energies for clusters of different charges

Since the emitted cluster ions are mostly populated within the m/z range <360 (regardless of charge polarities), fragmentation of clusters within this m/z range is most relevant. Table 2 summarizes the fragmentation pathways and threshold energies for these ions. Their neutral fragments consist of HEHN, HE, HNO_3, and H_2O. Interestingly, the positive and negative cluster ions of similar m/z not only eliminate neutral fragments of a similar (or the exact same) mass but also present the similar dissociation energies for these neutral losses.

The similarities in their fragmentation behaviors may be better reflected in Scheme 1, in terms of primary and secondary dissociation channels of positive and negative clusters. The combination of Table 2 and Scheme 1 reveal the following points: (1) elimination of HE and HNO_3 represents the major dissociation channel for small clusters. HNO_3 elimination is facile only in small clusters that contain 1–2 HEHN moieties and/or extra HNO_3, but becomes less favorable in large clusters as HNO_3 is encapsulated within a large assembly and stabilized by NO_3^-; (2) elimination of HEHN dominates in large clusters (this is consistent with ion-pair evaporation from large cluster ions of other ILs);[46] and dissociation of single and double HEHN is slightly more facile in positive clusters (by 0.4 eV) than in negative ones; and (3) water elimination is a major dissociation channel in the positive clusters but absent in the negative ones (due to the lack of extra $[HE + H]^+$). Related to this, N_2H_4-elimination was observed in the positive ion source whereas NH-elimination was observed in the negative ion source.

5.3 Cluster size dependence of dissociation energetics and intra-ion pair PT

The examination of HEHN and HE elimination enthalpies across the series of $[(HEHN)_nNO_3]^-$ provides further insight. Fig. 7a plots the precisely determined 0 K dissociation threshold energies based on the combination of LOC fitted experimental E_0 and DFT calculated ΔH (0 K). Since we were not able to obtain E_0 and ΔH (0 K) for every primary ion or every dissociation channel, another set of dissociation energy dependence *vs.* cluster size data is presented in Fig. 7b using *apparent threshold energies*. The apparent threshold energies were estimated by extending the tangents along the cross section rising sides to zero. We may not directly compare the data set of actual *vs.* apparent dissociation thresholds, but both sets present the same trends. The elimination energies of single and double HEHN decrease as the cluster size increases; whereas the elimination energy of HE, either by itself or accompanying HEHN, increases with the increasing size of the clusters.

To address the opposite size dependence for HE and HEHN elimination, Fig. 8 compares the reverse PT barrier for HEHN → HE·HNO_3 *vs.* the size/structure of host clusters. The barrier energetics was acquired from relaxed PES scans along the PT coordinate in a monomer and the reverse PT coordinate in a dimer. In the gas phase, a single HEHN monomer adopts a H-bonded HE·HNO_3 structure, but PT may be triggered over a barrier of less than 0.02 eV (or slightly exothermic depending on the calculation levels of theory). On the other hand, two dimeric structures may be considered, *i.e.*, HE·HNO_3·HEH^+·NO_3^- *vs.* $(HEH^+{\cdot}NO_3^-)_2$. The first structure is stable only at a

Table 2 Major dissociation pathways and energies in positive and negative cluster ions

Positive clusters	Fragments	ΔH (eV)	Negative clusters	Fragments	ΔH (eV)
$[(HE)_2 + H]^+$	$[HE + H]^+ + HE$	1.36	$[(HNO_3)NO_3]^-$	$NO_3^- + HNO_3$	1.38
$[CH_2CHNHNH_2{\cdot}HE + H]^+{\cdot}H_2O$ (m/z 153)	$[HE + H]^+ + CH_2CH_2NHNH_2 + H_2O$	1.47	(m/z 125)		
$[(HEHN)HE + H]^+$	$[(HE)_2 + H]^+ + HNO_3$	0.82	$[(HEHN)NO_3]^-$	$[(HNO_3)NO_3]^- + HE$	1.20
(m/z 216)	$(HE + H)^+ + HEHN$	1.42	(m/z 201)	$NO_3^- + HEHN$	1.80
$[(HEHN)(HE)_2 + H]^+$	$[(HEHN)HE + H]^+ + HE$	1.06	$[(HEHN)(HNO_3)NO_3]^-$	$[(HEHN)NO_3]^- + HNO_3$	0.92
(m/z 292)	$[(HE)_2 + H]^+ + HEHN$	1.09	(m/z 264)	$[(HNO_3)NO_3]^- + HEHN$	1.33
$[(HEHN)_2HE + H]^+$	$[(HEHN)(HE)_2 + H]^+ + HNO_3$	1.42	$[(HEHN)_2NO_3]^-$	$[(HEHN)(HNO_3)NO_3]^- + HE$	1.33
(m/z 355)	$[(HE)_2 + H]^+ + HEHN + HNO_3$	2.52	(m/z 340)	$[(HNO_3)NO_3]^- + HEHN + HE$	2.67
	$(HE + H)^+ + 2HEHN$	3.12		$NO_3^- + 2HEHN$	3.27

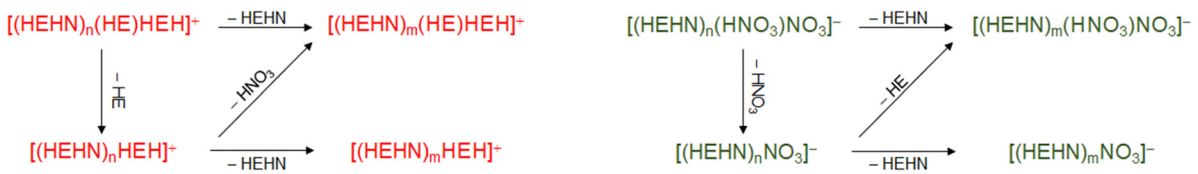

Scheme 1 Fragmentation patterns in positive (red) *vs.* negative (green) HEHN cluster ions.

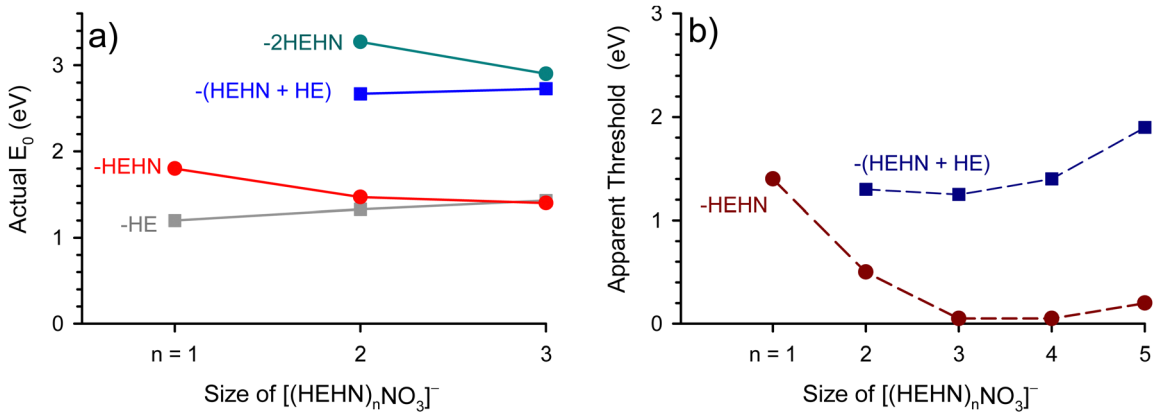

Fig. 7 Threshold energies for HE and HEHN elimination as a function of the $[(HEHN)_nNO_3]^-$ cluster size.

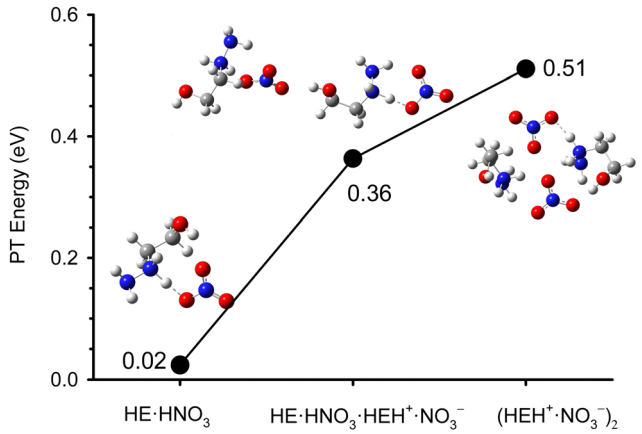

Fig. 8 Energy barrier for reverse proton transfer in different sizes and structures of $(HEHN)_{1-2}$, calculated at the ωB97XD/6-31+G(d,p) level of theory.

center-of-mass separation of ≥ 9 Å between the two HEHN moieties. The barrier for reverse PT is 0.36 eV in $HE{\cdot}HNO_3{\cdot}HEH^+{\cdot}NO_3^-$ but increases to 0.51 eV in $(HEH^+{\cdot}NO_3^-)_2$. The results support the findings in Fig. 7 that reverse PT becomes more unfavorable in the surrounding of HEHN ion-pair(s).

The same trend was observed for the PT-mediated HNO_3 elimination in the positive cluster ions,[37] *i.e.*, ΔH (0 K) is 0.82 eV for $[(HEHN)HE + H]^+ \rightarrow [(HE)_2 + H]^+ + HNO_3$ *vs.* 1.42 eV for $[(HEHN)_2HE + H]^+ \rightarrow [(HEHN)(HE)_2 + H]^+ + HNO_3$, and 0.83 eV for $[(HEHN)(HE)_2 + H]^+ \rightarrow [(HE)_3 + H]^+ + HNO_3$ *vs.* no HNO_3 elimination for $[(HEHN)_2(HE)_2 + H]^+$. This observation is consistent with a previous vibrational predissociation spectrum of corresponding D_2-tagged $(HEH^+)_2NO_3^-$ clusters,[36] wherein the observed strong, red-shifted feature at ~2310 cm^{-1} was assigned to the frustrated intermolecular PT of the acidic proton on the secondary amino group to the NO_3^- species in this cluster, while no feature was seen in the D_2-tagged $(HEH^+)_3(NO_3^-)_2$ cluster (which here corresponds to the $[(HEHN)_2HE + H]^+$ cluster above[37]). The spectrum of the latter in this region resembled that of the bulk condensed phase simulated by *ab initio* molecular dynamics. Furthermore, the trend in Fig. 8 will reach an asymptotic value for the PT barrier in the liquid phase ($HEHN_{(l)} \rightarrow HNO_{3(l)} + HE_{(l)}$).

6 Conclusions

Experimental and computational works are presented toward understanding the chemistry of 2-hydroxyethylhydrazinium nitrate clusters in different charge states. Mass spectrometry measurements were made to identify cluster ion compositions and to determine their dissociation product branching ratios, dissociation threshold energies, and dissociation rates (= cross section × relative velocity). These results were precisely matched to the explicit structures of primary cluster ions and fragments calculated using a combination of dynamics simulations and density functional theory. The major cluster ions formed in the negative charge state consist of $[(HEHN)_n(HNO_3)_{0-1}NO_3]^-$, the majority of which are populated within the *m*/*z* range of 62–340. Fragmentation of these cluster ions is dominated by the loss of neutral HEHN, HE, and HNO_3, of which the elimination of HE and HNO_3 require intra-ion pair proton transfer in the protic HEHN moiety and becomes difficult when the cluster size increases. Neutral loss results in an even narrower and lighter *m*/*z* distribution of cluster ions. These findings provide better knowledge of the various HEHN cluster stabilities and reaction thermodynamics. Comparisons to cluster formation and fragmentation in the positive charge state have revealed remarkable resemblances in terms of their similarities in *m*/*z* distributions, correlated compositions, fragmentation patterns, and threshold energies.

The existence of clusters is a defining feature of many ILs, playing a crucial role in IL-involved reactions and catalytic processes. This work highlights the distinctive IL clustering behaviors and micro-structures in the gas phase. It has particularly addressed the dominating ion-pair units within protic IL clusters at the molecular level, the intrinsic, solvent-free strengths of intra-ion pair electrostatic attraction, hydrogen bonding and the resulting intra-ion pair proton transfer. These interactions influence the assembly and evolution of clusters, as well as the mechanisms, kinetics, and dynamics of cluster breakup. These findings not only enhance our understanding

of IL chemistry but also guide the design and applications of ILs.

Data availability

The data supporting this article have been included as part of the ESI.†

Conflicts of interest

There are no conflicts to declare.

Acknowledgements

J. L. and W. Z. acknowledge the support of the Air Force Research Laboratory through Jacobs Technology Inc (Subcontract number RAPT1-0000001672). S. D. C. acknowledges support from the Air Force Office of Scientific Research under award number FA9300-20-F-9801.

References

1 D. R. MacFarlane, M. Kar and J. M. Pringle, *Fundamentals of Ionic Liquids: From Chemistry to Applications*, Wiley-VCH Verlag GmbH & Co. KGaA, Weinheim, Germany, 2017.
2 J. P. Hallett and T. Welton, *Chem. Rev.*, 2011, **111**, 3508–3576.
3 D. A. Fort, R. C. Remsing, R. P. Swatloski, P. Moyna, G. Moyna and R. D. Rogers, *Green Chem.*, 2007, **9**, 63–69.
4 W. M. Reichert, J. D. Holbrey, K. B. Vigour, T. D. Morgan, G. A. Broker and R. D. Rogers, *Chem. Commun.*, 2006, 4767–4779.
5 A. Avid, J. L. Ochoa, Y. Huang, Y. Liu, P. Atanassov and I. V. Zenyuk, *Nat. Commun.*, 2022, **13**, 6349.
6 H. Qi, Y. Ren, S. Guo, Y. Wang, S. Li, Y. Hu and F. Yan, *ACS Appl. Mater. Interfaces*, 2020, **12**, 591–600.
7 S. K. Shukla, S. G. Khokarale, T. Q. Bui and J.-P. T. Mikkola, *Front. Mater.*, 2019, **6**, 42.
8 X. Jin, L. Yu, D. Garcia, R. X. Ren and X. Zeng, *Anal. Chem.*, 2006, **78**, 6980–6989.
9 W. Gu, H. Chen, Y.-C. Tung, J.-C. Meiners and S. Takayama, *Appl. Phys. Lett.*, 2007, **90**, 033505.
10 K. Lunstroot, K. Driesen, P. Nockemann, C. Görller-Walrand, K. Binnemans, S. Bellayer, J. Le Bideau and A. Vioux, *Chem. Mater.*, 2006, **18**, 5711–5715.
11 A. Hammerl, G. Holl, M. Kaiser, T. M. Klapotke, R. Kranzle and M. Vogt, *Z. Anorg. Allg. Chem.*, 2002, **628**, 322–325.
12 M. Smiglak, A. Metlen and R. D. Rogers, *Acc. Chem. Res.*, 2007, **40**, 1182–1192.
13 S. Schneider, T. Hawkins, M. Rosander, G. Vaghjiani, S. Chambreau and G. Drake, *Energy Fuels*, 2008, **22**, 2871–2872.
14 S. Schneider, T. Hawkins, Y. Ahmed, M. Rosander, L. Hudgens and J. Mills, *Angew. Chem., Int. Ed.*, 2011, **50**, 5886–5888.
15 Y. Zhang and J. M. Shreeve, *Angew. Chem., Int. Ed.*, 2011, **50**, 935–937.
16 Q. Zhang and J. M. Shreeve, *Chem. Rev.*, 2014, **114**, 10527–10574.
17 P. D. McCrary, G. Chatel, S. A. Alaniz, O. A. Cojocaru, P. A. Beasley, L. A. Flores, S. P. Kelley, P. S. Barber and R. D. Rogers, *Energy Fuels*, 2014, **28**, 3460–3473.
18 R. Amrousse, T. Katsumi, N. Azuma and K. Hori, *Combust. Flame*, 2017, **176**, 334–348.
19 F. C. Gozzo, L. S. Santos, R. Augusti, C. S. Consorti, J. Dupont and M. N. Eberlin, *Chem. – Eur. J.*, 2004, **10**, 6187–6193.
20 P. J. Dyson, I. Khalaila, S. Luettgen, J. S. McIndoe and D. Zhao, *Chem. Commun.*, 2004, 2204–2205.
21 G. P. Jackson and D. C. Duckworth, *Chem. Commun.*, 2004, 522–523.
22 R. Bini, O. Bortolini, C. Chiappe, D. Pieraccini and T. Siciliano, *J. Phys. Chem. B*, 2007, **111**, 598–604.
23 A. M. Fernandes, J. A. P. Coutinho and I. M. Marrucho, *J. Mass Spectrom.*, 2009, **44**, 144–150.
24 Y. Fujiwara, N. Saito, H. Nonaka and S. Ichimura, *J. Appl. Phys.*, 2012, **111**, 064901.
25 B. D. Prince, B. A. Fritz and Y.-H. Chiu, *Ionic liquids: Science and Applications (ACS Symp. Ser.)*, American Chemical Society, 2012, vol. 1117, pp. 27–49.
26 S. W. Miller, B. D. Prince, R. J. Bemish and J. L. Rovey, *J. Propul. Power*, 2014, **30**, 1701–1710.
27 D. Krejci, F. Mier-Hicks, R. Thomas, T. Haag and P. Lozano, *J. Spacecr. Rockets*, 2017, **54**, 447–458.
28 A. L. Patrick, K. M. Vogelhuber, B. D. Prince and C. J. Annesley, *J. Phys. Chem. A*, 2018, **122**, 1960–1966.
29 A. L. Patrick, *Rapid Commun. Mass Spectrom.*, 2020, **34**, e8587.
30 J. L. Shamshina, M. Smiglak, D. M. Drab, T. G. Parker, H. W. H. Dykes, Jr., R. Di Salvo, A. J. Reich and R. D. Rogers, *Chem. Commun.*, 2010, **46**, 8965–8967.
31 T. W. Hawkins, A. J. Brand and G. W. Drake, *USA Pat.*, 20140190598, 2014.
32 A. Chowdhury and S. T. Thynell, *Propellants, Explos., Pyrotech.*, 2010, **35**, 572–581.
33 A. A. Esparza, S. D. Chambreau, G. L. Vaghjiani and E. Shafirovich, *Combust. Flame*, 2020, **220**, 1–6.
34 S. D. Chambreau, D. M. Popolan-Vaida, O. Kostko, J. K. Lee, Z. Zhou, T. A. Brown, P. Jones, K. Shao, J. Zhang, G. L. Vaghjiani, R. N. Zare and S. R. Leone, *J. Phys. Chem. A*, 2022, **126**, 373–394.
35 B. D. Prince, C. J. Annesley, R. J. Bemish and S. Hunt, *AIAA Propulsion and Energy 2019 Forum*, Indianapolis, IN, 2019.
36 H. J. Zeng, T. Khuu, S. D. Chambreau, J. A. Boatz, G. L. Vaghjiani and M. A. Johnson, *J. Phys. Chem. A*, 2020, **124**, 10507–10516.
37 W. Zhou, J. Liu, S. D. Chambreau and G. L. Vaghjiani, *Phys. Chem. Chem. Phys.*, 2023, **25**, 17370–17384.
38 M. J. Wainwright, J. L. Rovey, S. W. Miller, B. D. Prince and S. P. Berg, *J. Propul. Power*, 2019, **35**, 922–929.
39 S. W. Miller, B. D. Prince, R. J. Bemish and J. Rovey, *52nd AIAA/SAE/ASEE Joint Propulsion Conference*, Salt Lake City, UT, 2016.

40 D. A. Bonhommeau, R. Spezia and M.-P. Gaigeot, *J. Chem. Phys.*, 2012, **136**, 184503.
41 C. Miller and P. C. Lozano, *52nd AIAA/SAE/ASEE Joint Propulsion Conference*, Salt Lake City, UT, 2016.
42 N. M. Uchizono, A. L. Collins, C. Marrese-Reading, S. M. Arestie, J. K. Ziemer and R. E. Wirz, *J. Appl. Phys.*, 2021, **130**, 143301.
43 N. M. Uchizono, C. Marrese-Reading, S. M. Arestie, A. L. Collins, J. K. Ziemer and R. E. Wirz, *Appl. Phys. Lett.*, 2022, **121**, 074103.
44 F. Mier-Hicks and P. C. Lozano, *J. Propul. Power*, 2017, **33**, 456–467.
45 M. Breddan, A. Collins and R. Wirz, *The 36th International Electric Propulsion Conference*, Vienna, Austria, 2019.
46 J. F. de la Mora, M. Genoni, L. J. Perez-Lorenzo and M. Cezairli, *J. Phys. Chem. A*, 2020, **124**, 2483–2496.
47 C. E. Miller and P. C. Lozano, *Appl. Phys. Lett.*, 2020, **116**, 254101.
48 N. Nuwal, V. A. Azevedo, M. R. Klosterman, S. Budaraju, D. A. Levin and J. L. Rovey, *J. Appl. Phys.*, 2021, **130**, 184903.
49 L. Su, J. Zhuo, H. Liu, Z. Yao, X. Xu and S. Li, *Fuel*, 2023, **335**, 126919.
50 G. J. Van Berkel and F. Zhou, *Anal. Chem.*, 1995, **67**, 2916–2923.
51 P. Lozano and M. Martínez-Sánchez, *J. Colloid Interface Sci.*, 2004, **280**, 149–154.
52 P. Lozano and M. Martínez-Sánchez, *J. Colloid Interface Sci.*, 2005, **282**, 415–421.
53 A. Bruno, M. Schroeder and P. C. Lozano, *AIAA SCITECH 2022 Forum*, American Institute of Aeronautics and Astronautics, 2021.
54 L. Su, Z. Yao, J. Zhuo, H. Liu, H. Yan and S. Li, *Energy Fuels*, 2023, **37**, 13218–13230.
55 Y. Fang and J. Liu, *J. Phys. Chem. A*, 2009, **113**, 11250–11261.
56 W. Zhou, J. Liu, S. D. Chambreau and G. L. Vaghjiani, *Phys. Chem. Chem. Phys.*, 2022, **24**, 14033–14043.
57 M. Yamashita and J. B. Fenn, *J. Phys. Chem.*, 1984, **88**, 4671–4675.
58 F. M. Wampler, A. T. Blades and P. Kebarle, *J. Am. Soc. Mass Spectrom.*, 1993, **4**, 289–295.
59 F. Liu, W. Lu, X. Yin and J. Liu, *J. Am. Soc. Mass Spectrom.*, 2016, **27**, 59–72.
60 S. K. Chowdhury, V. Katta and B. T. Chait, *Rapid Commun. Mass Spectrom.*, 1990, **4**, 81–87.
61 T. Kim, K. Tang, H. R. Udseth and R. D. Smith, *Anal. Chem.*, 2001, **73**, 4162–4170.
62 K. Tang, A. V. Tolmachev, E. Nikolaev, R. Zhang, M. E. Belov, H. R. Udseth and R. D. Smith, *Anal. Chem.*, 2002, **74**, 5431–5437.
63 R. M. Moision and P. B. Armentrout, *J. Am. Soc. Mass Spectrom.*, 2007, **18**, 1124–1134.
64 A. N. Krutchinsky, I. V. Chernushevich, V. L. Spicer, W. Ens and K. G. Standing, *J. Am. Soc. Mass Spectrom.*, 1998, **9**, 569–579.
65 D. J. Douglas and J. B. French, *J. Am. Soc. Mass Spectrom.*, 1992, **3**, 398–408.
66 P. B. Armentrout, *J. Am. Soc. Mass Spectrom.*, 2002, **13**, 419–434.
67 C. Rebick and R. D. Levine, *J. Chem. Phys.*, 1973, **58**, 3942–3952.
68 R. D. Levine and R. B. Bernstein, *Molecular Reaction Dynamics and Chemical Reactivity*, Oxford University Press, New York, 1987.
69 P. B. Armentrout, *Int. J. Mass Spectrom.*, 2000, **200**, 219–241.
70 J. Liu, B. van Devener and S. L. Anderson, *J. Chem. Phys.*, 2002, **116**, 5530–5543.
71 M. M. Moe, J. Benny, Y. Sun and J. Liu, *Phys. Chem. Chem. Phys.*, 2021, **23**, 9365–9380.
72 P. J. Chantry, *J. Chem. Phys.*, 1971, **55**, 2746–2759.
73 C. Lifshitz, R. L. C. Wu, T. O. Tiernan and D. T. Terwilliger, *J. Chem. Phys.*, 1978, **68**, 247–260.
74 M. B. Sowa-Resat, P. A. Hintz and S. L. Anderson, *J. Phys. Chem.*, 1995, **99**, 10736–10741.
75 Y. Sun, M. M. Moe and J. Liu, *Phys. Chem. Chem. Phys.*, 2020, **22**, 14875–14888.
76 K. M. Ervin and P. B. Armentrout, *J. Chem. Phys.*, 1985, **83**, 166–189.
77 M. T. Rodgers, K. M. Ervin and P. B. Armentrout, *J. Chem. Phys.*, 1997, **106**, 4499–4508.
78 R. A. Marcus, *J. Chem. Phys.*, 1952, **20**, 359–364.
79 M. J. Abraham, T. Murtola, R. Schulz, S. Páll, J. C. Smith, B. Hess and E. Lindahl, *SoftwareX*, 2015, **1–2**, 19–25.
80 S. Páll, A. Zhmurov, P. Bauer, M. Abraham, M. Lundborg, A. Gray, B. Hess and E. Lindahl, *J. Chem. Phys.*, 2020, **153**, 134110.
81 M. J. Frisch, G. W. Trucks, H. B. Schlegel, G. E. Scuseria, M. A. Robb, J. R. Cheeseman, G. Scalmani, V. Barone, G. A. Petersson, H. Nakatsuji, X. Li, M. Caricato, A. V. Marenich, J. Bloino, B. G. Janesko, R. Gomperts, B. Mennucci, H. P. Hratchian, J. V. Ortiz, A. F. Izmaylov, J. L. Sonnenberg, D. Williams-Young, F. Ding, F. Lipparini, F. Egidi, J. Goings, B. Peng, A. Petrone, T. Henderson, D. Ranasinghe, V. G. Zakrzewski, J. Gao, N. Rega, G. Zheng, W. Liang, M. Hada, M. Ehara, K. Toyota, R. Fukuda, J. Hasegawa, M. Ishida, T. Nakajima, Y. Honda, O. Kitao, H. Nakai, T. Vreven, K. Throssell, J. A. Montgomery Jr., J. E. Peralta, F. Ogliaro, M. J. Bearpark, J. J. Heyd, E. N. Brothers, K. N. Kudin, V. N. Staroverov, T. A. Keith, R. Kobayashi, J. Normand, K. Raghavachari, A. P. Rendell, J. C. Burant, S. S. Iyengar, J. Tomasi, M. Cossi, J. M. Millam, M. Klene, C. Adamo, R. Cammi, J. W. Ochterski, R. L. Martin, K. Morokuma, O. Farkas, J. B. Foresman and D. J. Fox, *Gaussian 16*, Gaussian, Inc., Wallingford, CT, 2016, vol. Rev. D.01.
82 T. Lu, *Sobtop*, Beijing Kein Research Center for Natural Sciences, Beijing, 2023, vol. 1.0.
83 O. Ghasemalizadeh, S. Khaleghian and S. Taheri, *Int. J. Adv. Res.*, 2016, **4**, 1668–1686.
84 W. Humphrey, A. Dalke and K. Schulten, *J. Mol. Graphics*, 1996, **14**, 33–38.
85 K. K. Baldridge, M. S. Gordon, R. Steckler and D. G. Truhlar, *J. Phys. Chem.*, 1989, **93**, 5107–5119.

86 W. L. Hase, *Advances in Classical Trajectory Methods, Intramolecular and Nonlinear Dynamics*, JAI, Greenwich, Conn., 1992, vol. 1.
87 K. Bolton, W. L. Hase and G. H. Peslherbe, in *Modern Methods for Multidimensional Dynamics Computations in Chemistry* ed. D. L. Thompson, World Scientific, Singapore, 1998, pp. 143–189.
88 V. Bakken, J. M. Millam and H. B. Schlegel, *J. Chem. Phys.*, 1999, **111**, 8773–8777.
89 L. Sun and William L. Hase, *Rev. Comput. Chem.*, 2003, **19**, 79–146.
90 X. Hu, W. L. Hase and T. Pirraglia, *J. Comput. Chem.*, 1991, **12**, 1014–1024.
91 W. L. Hase, K. Bolton, P. de Sainte Claire, R. J. Duchovic, X. Hu, A. Komornicki, G. Li, K. Lim, D. Lu, G. H. Peslherbe, K. Song, K. N. Swamy, S. R. Vande Linde, A. Varandas, H. Wang and R. J. Wolf, *VENUS 99: A General Chemical Dynamics Computer Program*, Texas Tech University Lubbock, TX, 1999.
92 G. H. Peslherbe, H. Wang and W. L. Hase, *Adv. Chem. Phys.*, 1999, **105**, 171–201.
93 C. Larriba and C. J. Hogan, Jr., *J. Comput. Phys.*, 2013, **251**, 344–363.
94 C. Larriba-Andaluz and C. J. Hogan, Jr., *J. Chem. Phys.*, 2014, **141**, 194107.
95 J. Liu, W. Zhou, S. D. Chambreau and G. L. Vaghjiani, *J. Phys. Chem. B*, 2019, **123**, 2956–2970.
96 J. Liu, W. Zhou, S. D. Chambreau and G. L. Vaghjiani, *J. Phys. Chem. B*, 2020, **124**, 4303–4325.
97 W. Zhou, J. Liu, S. D. Chambreau and G. L. Vaghjiani, *J. Phys. Chem. B*, 2020, **124**, 11175–11188.
98 I. M. Alecu, J. Zheng, Y. Zhao and D. G. Truhlar, *J. Chem. Theory Comput.*, 2010, **6**, 2872–2887.
99 E. Paenurk and P. Chen, *J. Phys. Chem. A*, 2023, **128**, 333–342.